J MATER SCI **41** (2006) 2691–2702

The weak-beam technique applied to the analysis of materials properties

P. VEYSSIÈRE
LEM, CNRS-ONERA, BP 72, 92322, Chatillon, France

Published online: 17 April 2006

The so-called weak-beam (WB) technique has been widely employed to elucidate dislocation near-core properties. To a very large extent WB images reflect the intimate structure of lattice defects through signals that may, however, be significantly convoluted. This contribution reviews selected situations where various factors affecting images must be taken into account. A less-common method to investigate crystal order under WB is also reported.

1. Introduction

Dislocation analysis by transmission electron microscopy (TEM) under diffraction contrast, including *in situ* straining experiments, is one of the fields Hiroyashu Saka has significantly contributed to. Saka was first to point out that, in practice, the detrimental effects of crystal anisotropy on dislocation identification can be avoided provided one operates under weak-beam conditions [1]. All that one could do before that was to produce a number of images simulated under all possibly relevant dynamical bright/dark-field conditions and to try to figure out which candidate Burgers vector(s) would provide optimized image consistency with a variety of butterfly-wing-like images. Saka's remark, which may appear as rather petty to a researcher unfamiliar with the issue, has immensely facilitated subsequent dislocation investigations in highly anisotropic materials such as minerals and intermetallic alloys. In addition to straightforward Burgers vector identification, this has also enabled direct, experimental access to dislocation fine structure in anisotropic metals with no special expertise required other than being able to produce a weak-beam image, which is actually quite trivial.

In recognition of the impact of Saka's contributions to the field, this paper will review selected achievements in dislocation analysis at core level with attention paid to the extent dislocation core structure is or is not reflected under WB conditions, and to the implications of this. In a first part though, and because in the author's view this is somewhat inadequately addressed in textbooks and review articles, some principles of the WB method and suitable experimental procedures will be summed up (Section 2). Section 3 elaborates on some general properties of dislocation images. Section 4 will discuss applications of the WB method to measuring distances between dislocations. Finally, Section 5 accounts for a particular use made of weak beams to investigate crystal order.

2. The weak-beam method: principles and practical knacks

"Weak-beam" refers to imaging under diffraction contrast with a reflection **g** set far off the Bragg condition. It is only from crystal volumes where lattice distortion is enough to restore that particular Bragg condition locally that a visible, bright signal emerges from an otherwise faint background.

2.1. Resolution under weak beam

The weak-beam peak can be regarded as arising from the constructive interference of the waves originating from several scattering atoms (Fig. 1), thence resolution under WB is related to the number of atoms actually needed to generate a detectable peak. For that simple reason, resolution cannot be thought of as being less than 3 to 4 atomic distances, that is, almost one order of magnitude larger than the nominal resolution of the latest generations of electron microscopes. It is worth noting that the resolution of weak-beam images is thus not instrument limited. Yet, in setting up imaging conditions in the microscope one should keep in mind that inelastically scattered electrons may blur images significantly and that every time the objective aperture, the deflection coils and sample position in the objective pole piece have been touched, then objective astigmatism is to be corrected for.

The larger the excursion from the Bragg condition under reflection **g**, as measured by the deviation parameter

0022-2461
DOI: 10.1007/s10853-006-7872-1

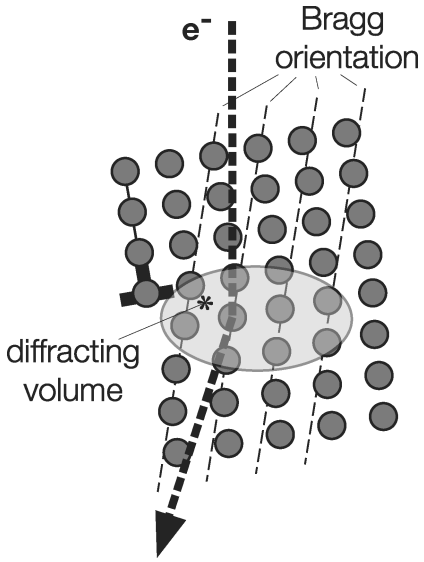

Figure 1 The weak-beam signal is engendered in the highly distorted vicinity of a dislocation where several atoms are locally in Bragg positions for the incident beam.

$s_{\mathbf{g}}$, the greater the distortion required to restore this Bragg condition. Since lattice rotation is conversely proportional to the distance to the core, the image of a dislocation is, as $s_{\mathbf{g}}$ is increased, shifted toward the geometrical projection of the dislocation core in the diffracted direction. Images narrow accordingly but since the peak intensity fades rapidly out (as ${s_{\mathbf{g}}}^{-2}$), limitations in imaging defects arise soon. It should be realized that however close a dislocation image is to the geometrical projection of the dislocation core, there is in principle no coincidence between them (see however [2, 3]). Existing shifts may be further influenced by close-by distortion-generating centres such as in dissociated configurations or in subboundaries.

2.2. Weak-beam conditions

Some confusion remains in the literature as to what adequate or standard weak-beam conditions should be which returns us to early contributions (for a review see [4]). The WB imaging technique was made available at a time where, for lack of precise knowledge on dissociation widths in certain model crystals, theoretical analyses of dislocation properties involving cross-slip could not be accounted for with reasonable confidence. It could not be ascertained for instance whether dislocations in silicon were dissociated.

It is worth keeping in mind that the so-called "weak-beam" conditions have been devised from computer-generated profiles and not from real situations and this is because the faintest signals to be seen on a fluorescent screen were generally far too strong to qualify for the remotest weak-beam condition. The simulated profiles indicated that in order to be able to resolve the peaks of two companion Shockley partials in Cu with the microscope, one should make sure that

(i) $s_{\mathbf{g}}$, the deviation from the Bragg condition (in the defect-free volume) be more than 0.2 nm^{-1},
(ii) $\mathbf{g.b} \leq 2$ to avoid extra peaks ($\mathbf{b}$ is the Burgers vector of the parent, undissociated dislocation),
(iii) the product $s_{\mathbf{g}}\ \xi_{\mathbf{g}}$ be larger than 5 to ensure good contrast (where $\xi_{\mathbf{g}}$ is the extinction distance for the family of diffracting planes considered) and
(iv) no reflection is strongly excited.

These conditions are specific a given combination of crystal parameter (that of copper) and extinction distance ($\mathbf{g} = 220$). The so-called "weak-beam" conditions given above are, in addition, strictly applicable to the current operating voltage, 100 kV, at the time these conditions were prescribed. The situation has of course considerably evolved since [5]. The variety of crystals investigated so far covers a wide range of cell parameters (e.g. $\sim$ up to 1.3 nm in garnets), the standard operating voltage turns out to be 200 kV. Most importantly, the dislocation properties tackled in TEM have widened beyond the initial measurements of dissociation distances, that is, of stacking-fault energies in crystals [6]. Last but not least, image intensifiers have made it possible to work under fairly weak signals, recording times have shortened considerably (at least one order of magnitude between the times to expose regular and imaging plates) and instrumental drifts have been cut down. As a result, instead of the stringent and too specific conditions (i)–(iv) above, the following flexible recommendations can be followed with appreciable benefit in most cases:

(a) image adjustment should be concluded whenever the resolution adequate to tackle a given situation is attained, with the restriction that
(b) for the defect under investigation, every contrast peculiarity in the image(s) makes sense (see also [5]).

Should some doubt arise in interpreting specific contrast properties, such as the unexpected appearance/disappearance of certain partials, more (fewer) than expected peaks—all illustrated in the following sections,—then one should have recourse to image simulation which usually fixes the problem. For this reason, the restriction to $\mathbf{g.b} \leq 2$ is unnecessary if not somewhat unrealistic in certain crystals (e.g. $\mathbf{g.b} = 4$, for $\mathbf{g}$ parallel to $\mathbf{b}$ in spinel). On the other hand, although $s_{\mathbf{g}} \sim 0.2\ nm^{-1}$ is not inappropriate in many standard cases, recommendation (a) makes a deviation as large as 0.2 nm^{-1} uselessly stringent in practice. This is so, for instance, in the case of widely separated partials or else when comparing microstructural properties after various deformation conditions, in which case all is needed is a wholesale view of dislocation organization and/or preferred dislocation

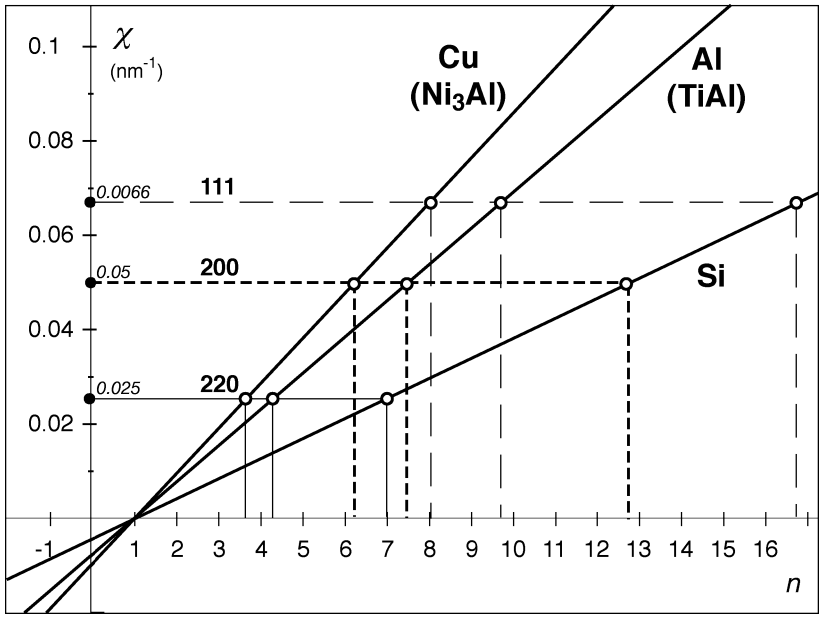

Figure 2 Chart of $\chi = (n-1)\,\lambda/(2\,a^2)$ versus n in Al, Cu and Si (see Equation 1). Since χ is also equal to $s_{\mathbf{g}}/(h^2 + k^2 + l^2)$, the values of n to achieve $s_{\mathbf{g}} = 0.2\ \mathrm{nm}^{-1}$ for $\mathbf{g} = 111$, 200 or 220 come out as the intersections of the three inclined thick lines (for Cu, Al and Si) by horizontal lines at $\chi = 0.066$, 0.05 and 0.025 respectively. The lattice parameters of Ni_3Al and TiAl are within 1% of those of Cu and Al, respectively.

directions. A good weak-beam image of a microstructural organization is as difficult, if not less so, to set up than the same under dynamical conditions and this weak-beam image imparts far more information than the regular bright- or dark-field image of the same area. There are of course situations where $s_{\mathbf{g}}$ needs to be increase beyond $0.2\ \mathrm{nm}^{-1}$.

The deviation $s_{\mathbf{g}}$ can be measured from the coordinate n (in units of $\mathbf{g}$) where the Ewald sphere intersects the systematic row. It is written

$$s_{\mathbf{g}} = (n-1)\mathbf{g}^2\,\lambda/2 \qquad (1)$$

where λ is the electron wavelength. The coordinate n is utilized in the convenient $(\mathbf{g} - n\mathbf{g})$ notation often used to define a given imaging condition. That can be equivalently given from the coordinate, $n/2$, of the projection of the centre of the Ewald sphere on the systematic row. The knowledge of n does not facilitate comparisons between materials. Fig. 2 shows that in order to attain $s_{\mathbf{g}} = 0.2\ \mathrm{nm}^{-1}$, in Cu, Al and Si under say the 200 reflection, one needs to set n at 6.2, 7.4 and 12.7, respectively. Adequate deviations from the Bragg conditions, tested on a number of crystals such as Cu, Al, Si and intermetallic alloys, e.g. Ni_3Al, TiAl, are such that n usually lies in the ranges 2.5–7, 4–10 and 6–12 for the 220, 200 and 111 reflections, respectively. It is clear that the $(\mathbf{g} - 3\mathbf{g})$ condition which has often been employed to generate WB images in a variety of materials, is rather difficult to justify.

In practice, rather than satisfying a given set of imaging parameters, one should prefer conducting the final adjustments in the image mode under the selected reflection, and that includes correction for astigmatism. In the course of routine observations, there is no need to measure $s_{\mathbf{g}}$ accurately unless recourse to simulation is expected. It is actually far more efficient to check the image preferably to the diffraction pattern, and to adjust image quality to the problem tackled. This is preferably achieved directly from a TV monitor after image intensification, a pivotal equipment in weak-beam imaging, making sure that no contrast artifact is accidentally introduced. As illustrated in the following, counterintuitive effects may occur though, and this makes it useful if not indispensable to check *in situ* still whether or not a given unusual feature is stable against slight changes in $s_{\mathbf{g}}$. Note that reflections seldom used because of their relatively poor structure factors are worth trying. For instance, 224 reflections in fcc-based TiAl produce useful weak-beam images.

3. Image properties

A recurrent issue arises from the fact that weak-beam images usually reflect the defect fine structure far too well. This can be misleading for images are sometimes examined (i) as if there were a one-to-one geometrical correspondence between what one sees and the real defect and (ii) as if image intensities could unambiguously inform on Burgers vectors.

3.1. Peak position

For obvious reasons, dissociation distances should be measured with the best possible precision and that in turn

implies that the position of dislocation peaks can be reliably predicted.

3.1.1. The CRW criterion

Cockayne, Ray and Whelan (CRW) [7] have proposed an approximate derivation of the image shift between the true projection of a dislocation and the position of the weak-beam peak, predicting that the latter will arise from crystal regions where

$$\partial[\mathbf{g}.\mathbf{R}(x, z)]/\partial z = -s_g \tag{2a}$$

and

$$\partial^2[\mathbf{g}.\mathbf{R}(x, z)]/\partial z^2 = 0 \tag{2b}$$

where condition (2a) reflects the fact that at $\mathbf{R}(x, z)$, the local lattice rotation restores a departure $s_\mathbf{g}$ from the Bragg condition while condition (2b) ensures that (2a) is satisfied over some distance along the direction of the incident beam. The longer this distance, the brighter the signal. How long should (2a) and (2b) be simultaneously satisfied along a column in order to supply a visible peak is, however, not part of the criterion as it is actually hard to assess quantitatively. In many instances, the CRW criterion has proved an extremely useful guideline (see Section 3.4) but it has inherent limitations that have been quite extensively discussed.

The mechanisms involved in the formation of a weak-beam image are indeed not as entirely straightforward as hypothesized for the derivation of the CRW criterion. Howie *et al*. [8] have shown that, because of possible interband transitions in the dispersion surface (see also [9]), condition (2) is only a rough approximation for predicting image position. At the origin of the peak shift existing between a dislocation and its image is the rapidly varying distortion field next to the dislocation core that may restore Bragg conditions for reflections other than **g** and that encourage dynamical scattering locally. It is interesting to note that even numerical simulations are not totally unambiguous since the outcome depends on the approach employed to account for the interactions of electrons with a defected crystal (see Fig. 11 in [8]), and that may include whether or not the so-called column approximation is taken into account [10].

It is for example postulated (see [11], p. 218) that in the Bloch wave formulation of the dynamical theory, the crystal potential can be re-written in the deformable ion approximation (i.e. $V(\mathbf{r}) \rightarrow V(\mathbf{r} - \mathbf{R}(\mathbf{r}))$, an assumption which is valid only if the crystal potential deforms smoothly. In fact the formulation is said to be applicable provided $\mathbf{R}(\mathbf{r})$ does not change significantly in a lattice distance. This is true at some distance from the core, that is, for 'dynamical' dislocation images, when a large volume of the crystal can be regarded as roughly perfect and translated uniformly by **R**. For the above-mentioned standard value of $s_\mathbf{g} = 0.2\ \mathrm{nm}^{-1}$ in weak-beam, an order of magnitude for $\partial\,|\mathbf{R}|/\partial z$ is given by $\partial R_\mathbf{g}/\partial z = 0.2/|\mathbf{g}|$ where $R_\mathbf{g}$ is the projection of **R** on **g**. $\partial R_\mathbf{g}/\partial z$ amounts to a few per cent, actually a significant distortion for which the above approximation is therefore arguable. A similar remark may apply to the treatment the position-dependent perturbation of the perfect crystal potential by a lattice defect (see [8]). It is in effect unclear why, in the highly distorted region of interest for image formation under weak-beam conditions, this can still be regarded as a perturbation.

What these considerations suggest is that numerical simulations of weak-beam images should be utilized with some care since they may not always provide an accurate quantitative answer. Which theoretical approach, that is, which approximation, is best suited to this aim has not been convincingly discussed yet.

3.1.2. Graphical analysis

Certain of the above considerations on image shift are better understood from the plot of the locus of points defined by $(\partial\mathbf{g}.\mathbf{R}(x, z)/\partial z) = -s_\mathbf{g}$ with the vertical axis taken along z and the dislocation along y perpendicular to the page (Fig. 3) [12, 13]. The CRW conditions are obviously satisfied wherever the tangent to the curve is vertical, along the beam. Fig. 3 summarizes most of the effects of interest in the cases of an undissociated edge dislocation in Al and of a hypothetically undissociated dislocation in Cu ($s_\mathbf{g} = 0.2\ \mathrm{nm}^{-1}$, **g** is parallel to **b**). The envelopes of the lobes located in the $x \geq 0$ and $x \leq 0$ regions and passing through $\{x = 0, z = 0\}$ represent condition (2a) for

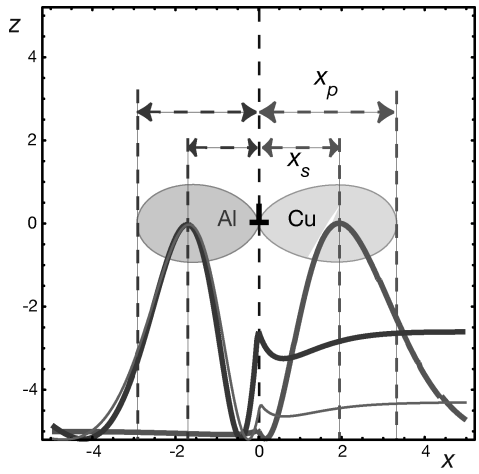

Figure 3 Contour plots of Equation 1 resolved under the anisotropic elasticity approximation for an undissociated dislocation in Al ($s_\mathbf{g} = -0.2\ \mathrm{nm}^{-1}$) and Cu ($s_\mathbf{g} = 0.2\ \mathrm{nm}^{-1}$). The z coordinate is taken along the electron beam. The origin of coordinates is at the dislocation core. The corresponding two-beam weak-beam simulated profiles are superimposed for comparison with the same scale along x. The thin curve on the Al side corresponds to an 8-beam simulation. It is noted that the simulated image is rather stable with respect to the number of beams incorporated in the simulation.

Al and Cu, respectively (at variance from Al, Cu exhibits some elastic anisotropy). The thick profiles are computed under the two-beam approximation. In Cu, the simulated image peaks at a distance x_s to the dislocation core that is smaller than that the shift, x_p, predicted from conditions (2). The difference is quite significant amounting for example to $x_p - x_s = 1.3$ nm in Cu when $x_s = 1.9$ nm, and $x_p - x_s = 1.2$ nm in Al when $x_s = 1.7$ nm. The thin profile that peaks in the $x \leq 0$ Al side is calculated using eight beams of the systematic row with the imaging conditions unchanged otherwise. There is no significant difference between the 2-beam and 8-beam cases. In each of the profiles shown in Fig. 3, the faint peak is consistent with the 'core peak' effect which, as demonstrated by Humphreys *et al.* [14], is always located at $x = 0$.

In addition to the effects discussed in the previous section, volume changes may play a role in defining the peak position. In the zone where image formation is expected to take place under weak-beam conditions, that is, within several b from the dislocation core, the crystal is markedly compressed in places and dilated in others. Under the simplistic, optical viewpoint of an image formed by local constructive interference from a few scattering atoms, the Bragg law cannot be satisfied where $s_{\mathbf{g}}^{\text{local}}$ is expected to cancel out under the kinematical incidence defined by $s_{\mathbf{g}} = 0.2\ \text{nm}^{-1}$. An order of magnitude of $\partial u_x/\partial x$ within $5b$ from the core of an edge dislocation is 1% (u_x is the displacement along the Burgers vector of a dislocation whose glide plane is parallel to the foil) corresponding to a noticeable fraction of the Bragg angle.

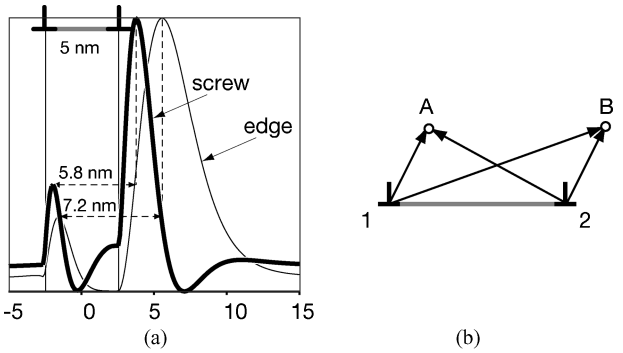

Figure 4 The markedly asymmetric image profile of a pair of partials with identical Burgers vectors. (*a*) screw and edge 1/2[110] partials (thick and thin lines, respectively) in Ni_3Al. The partials border an APB, not visible under the fundamental $\mathbf{g} = 220$ operating reflection, $s_{\mathbf{g}} = 0.2\ \text{nm}^{-1}$. The peak shifts together with the differences between the real separation (5 nm in both cases) and the peak separations should be noted. The foil normal is nearly parallel to the beam direction and to the normal to the (111) slip/dissociation plane of the dislocation. (*b*) the peak asymmetry originates from the fact that lattice rotations are not the same at A and B.

3.2. Burgers vector analysis

Before entering the question of Burgers vector analysis by contrast considerations of dislocation images, it is worth recalling that in wedge-shaped samples and for dislocations inclined to the foil, the scalar product **g.b**, including its sign, can be determined from the number, p, of thickness fringes terminating at the point of emergence of the dislocation [15]. This property has been applied to several concrete cases and its limitations discussed [16, 17].

Consider now a pair of parallel dislocations with identical 1/2[011] Burgers vectors, as is the case in a number of intermetallic alloys with an fcc-based structure where those pairs are interconnected by an antiphase boundary (APB). **g.b** being the same for both partials, one would expect them to exhibit similar intensities, a property which is true only for large separation distances. This is illustrated in Fig. 4a showing the computed image profile of a pair of partials interconnected by an APB, 5 nm wide. The configuration is nearly parallel to the projection plane. One sees that the profile is markedly asymmetric. There is a mirror plane at $x = 0$ between the two images for $\pm s_{\mathbf{g}}$ (not shown). As sketched in Fig. 4b where points A and B are located at equivalent positions for dislocations 1 and 2, respectively, the origin of the asymmetry is rather straightforward since $\mathbf{r}_{2A}$ differs from $\mathbf{r}_{1B}$ even though $\mathbf{r}_{1A} = \mathbf{r}_{2B}$, thus implying different lattice rotations at points A and B. This intrinsic profile asymmetry must be kept in mind when investigating dissociation modes [18]. For instance, there has been a debate as to which of the following dissociation schemes

$$\langle 011 \rangle \rightarrow 1/2\langle 011 \rangle + \text{APB} + 1/2\langle 011 \rangle \qquad (3)$$

$$\langle 011 \rangle \rightarrow 1/3\langle 112 \rangle + \text{SF} + 1/3\langle 121 \rangle \qquad (4)$$

prevails in certain $L1_2$ ordered alloys (SF stands for a stacking fault). To discriminate between the two reactions, comparing the peak relative intensities may be misleading and, instead, one needs a complete set of weak-beam images. This is shown in Fig. 5 in the case of TiAl ($L1_0$ structure). The choice of TiAl, whose unit cell is compatible with reactions (3) and (4), will enable a comparison of the above two reactions with reaction (5) below. The image of configuration (3) is again asymmetrical (Fig. 5a), as is the case for the image of configuration (4) (Fig. 5b). Incidentally, it is noted that the profiles in Fig. 5a can be entirely superimposed to those of Fig. 5b which is due to the fact that, under the imaging conditions chosen here (**g** parallel to $\mathbf{b} = [011]$), the partials are all imaged under the same value of $\mathbf{g.b}_{\text{partial}}$ (i.e. either 2 or -2). Hence, for reactions (3) and (4) to be distinguished it is necessary to check whether companion partials can be set out of contrast separately. It is an entirely general rule that to infer Burgers vectors of dislocation partials one should not rely on differences in the relative peak intensities.

In practice, a rather unusual case of an image asymmetry is provided by TiAl (Fig. 6). Neither reaction (3) and (4) is actually consistent with observations in this case since, under **g** parallel to the screw orientation and under

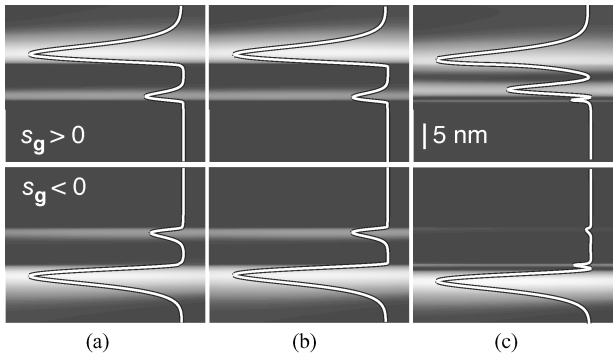

Figure 5 Simulated weak-beam images and corresponding profiles of a 60° dislocation in TiAl (**b** = [011]) for various hypothesized dissociation modes. (a) reaction (3). (b) reaction (4). (c) reaction (5). The diffraction vector **g** is parallel to the Burgers vector of the undissociated dislocation; each column shows the same configuration under $s_g = \pm 0.2\ \mathrm{nm}^{-1}$.

a given sign of the (s_g **g.b**) product, two partials with comparable intensities are observed (Fig. 6a) whilst one of the fades out upon reversal of this sign (Fig. 6b). As demonstrated by the entire consistency between observations and image simulations (Fig. 5), all covering a large variety of imaging conditions [19], this behaviour arises from the following dissociation mode

$$\langle 011 \rangle \rightarrow 1/6\ <112] + \mathrm{SISF} + 1/6\ <154] \qquad (5)$$

where SISF stands for superlattice intrinsic SF. Reflecting the tetragonal symmetry of TiAl, the $<hkl]$ notation allows every permutation between h and k while $\pm l$ is ascribed the third position. In Fig. 5c the 1/6 <112] and 1/6 <154] partials are located above and below and viewed under $|\mathbf{g.b}| = 1$ and 3, respectively. The unusual contrast behaviour observed here stems from the property of image asymmetry discussed above which, under the appropriate sign of s_g **g.b**, enhances the image of one partial to the expense of its companion's and conversely. What happens is that when conditions favour the peak of the 1/6 <112] partial (imaged under $|\mathbf{g.b}| = 1$), then that of its companion ($|\mathbf{g.b}| = 3$) is attenuated and both fall at about the same level. By contrast, when conditions favour the peak of the 1/6 <154] partial, its companion's is weakened so dramatically that is nearly invisible. In Fig. 5c one may notice the faint sub-peak that appears in the image of the lower 1/6 <154] partial regardless of whether s_g is positive or negative. This sub-peak is consistent with the fact that this partial is viewed under $|\mathbf{g.b}| = 3$ (see Fig. 7.17 in [11]). The generation of elongated faulted dipoles (FD in Fig. 6c) is amongst the many implications of this last dissociation reaction for this is encouraged when the 1/6 <154] partial is trailing, and hampered otherwise [20]. It has been accordingly predicted that FD production should be markedly stress-orientation dependent and this is fully confirmed by experiments [21]. Incidentally, why, in spite of certain analogies between the two ordered structures,

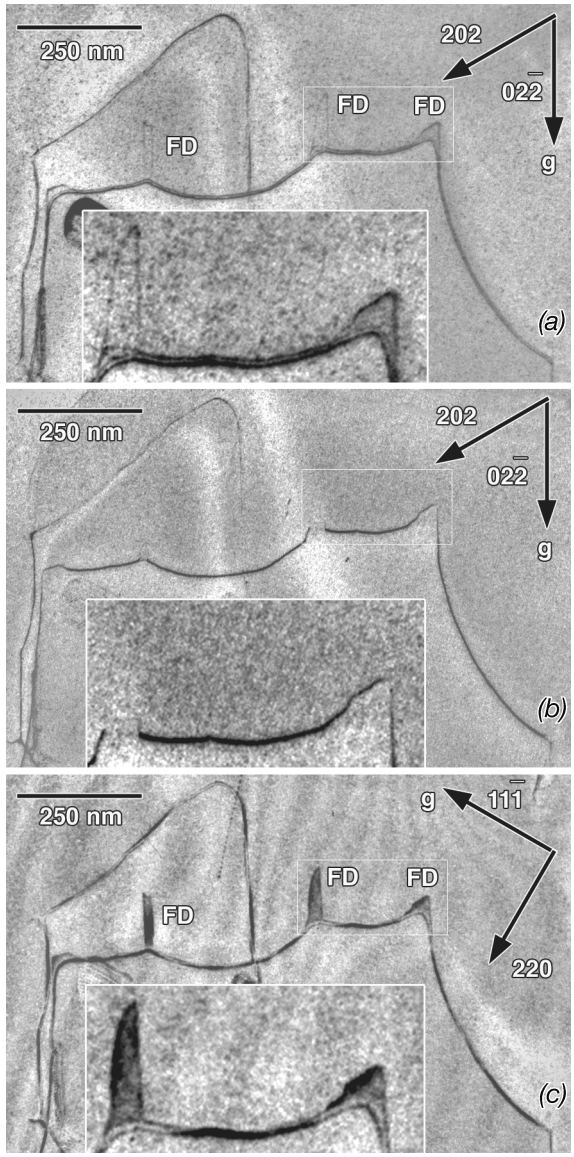

Figure 6 A weak-beam observation in TiAl attesting to the dissociation of a dislocation according to reaction (5). Under **g** = 022, the image shows two peaks with comparable intensity, while one of the two peaks disappears as the sign of s_g **g.b** is reversed. (Courtesy Dr Grégori).

faulted dipoles comprise an intrinsic stacking fault and an extrinsic in Ni_3Al and TiAl, respectively, remains mysterious to the present author. This point should deserve a systematic investigation in Ni_3Al in the vein of that conducted by Hemker and Viguier in TiAl [22].

Finally, it is worth recalling that a computer investigation of dislocation contrast under weak-beam conditions, and in particular of extinction conditions, is not all straightforward. It requires that a set of simulated images be compared, hence that these images are all generated under a common intensity scale. Deciding whether or not a simulated weak-beam image is visible, faint or invisible is relatively easy under dynamical conditions where the maximum intensity is that of the background. It is hardly

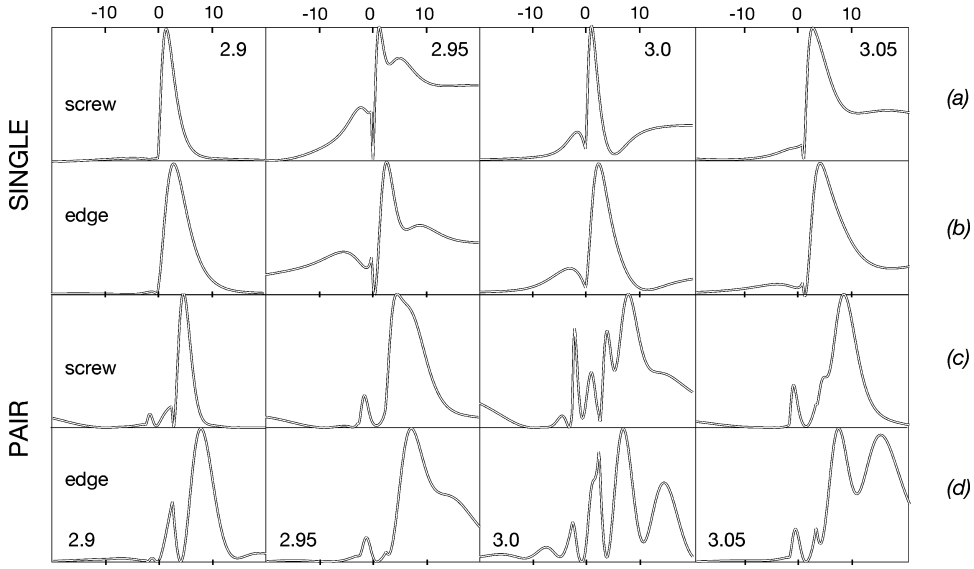

Figure 7 Simulated images and profiles of a single dislocation in Al, $\mathbf{g} = 220$ parallel to $\mathbf{b} = 1/2[110]$ under weak-beam conditions in the vicinity of the **g**-3**g** condition.

possible when the background is black and no fixed reference level for a maximum is available (the computed height of a dislocation peak under weak beam may vary by several orders of magnitude). This difficulty was the main reason why a valid analysis of the weak-beam contrast of partial dislocations had not been made available for fractional values of **g.b** although this has obvious practical interest in fcc and hcp metals, in a wide range of ordered alloys, as well as in semiconductors with diamond structure. For several decades, all what one could make use of was (i) extinction rules that had been derived from simulations carried out on fractional **g.b** values under dynamical conditions [23] and whose relevance to weak-beam images is to be ascertained or else (ii) considerations on peak intensity which, as seen above, can reveal quite misleading (see however [24]). A method for comparing weak-beam images has been designed a few years ago [25], it mimics that employed to calibrate image plates and it is made available in the CUFOUR package [26]. Yet, the conditions of visibility/invisibility of dislocation partials (under $\mathbf{g.b} = +1/3, +2/3$, etc. . .) remain to be established.

In summary for this section, peak intensity may not always inform on **g.b**, hence on **b**, and this remains true for relative peak intensities between companion partials.

3.3. Multiple images

In some cases a double peak may be mistakenly interpreted as attesting to a truly split dislocation. Multiple images under either a 200 or a 220 reflection have been reported in intermetallic alloys for a pair of dislocations with identical Burgers vectors ($\mathbf{b} = 1/2 <110>$ in $L1_2$ alloys) connected by an APB (Ni_3Al [27], Co_3Ti [28]; C.B. Carter and P. Veyssière: unpublished results). A similar property has been identified in NiAl (B2, bcc-related ordered structure) for two families of Burgers vectors, $<111>$ and $<100>$, imaged in the same area under the same weak-beam condition [29]. In every case where this has been tried, a slight excursion from the exact range of $s_{\mathbf{g}}$ values where image splitting occurs (e.g. next to **g**-3**g** in L12 alloys) was enough to restore an artifact-free image.

For clarity, we investigate this effect for an isolated, undissociated dislocation in the case of Al with $\mathbf{b} = 1/2[110]$ imaged under $\mathbf{g} = 220$, that is, when $\mathbf{g.b} = 2$ for no extra peak is then expected from the two-beam approximation (see Fig. 7.17 in [11]). Images of this dislocation are presented Fig. 7a and b where it is seen that, as $s_{\mathbf{g}}$ is varied, a secondary image appears and disappears around $n = 2.95$–3. For n lower than 2.9 or larger than 3.1 the dislocation peak is single and well defined. The same simulation again conducted in Al on a hypothetical pair of dislocations with $\mathbf{b} = 1/2[110]$ located at 5 nm of each other in the glide plane shows a similar far more pronounced effect of image splitting for $n = 3 - 3.05$ (Fig. 7c and d). A similar numerical test conducted in Ni_3Al with the above configuration indicates that the effect is not clearly dependent upon elastic anisotropy. What counts though is the number and the nature of the beams involved in the simulation since the splitting never appears in the two-beam simulations whereas it disappears from eight-beam images when the 440 reflection is removed.

3.4. Elastically anisotropic crystals

As mentioned earlier, image complexity in crystals with large anisotropy ratios makes dislocation identification under dynamical bright-or dark-field conditions impossible in practice without the support of extensive image

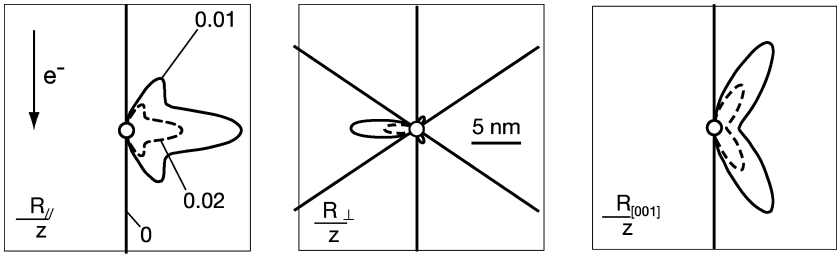

Figure 8 Contour maps of $\mathbf{u}.(\partial\mathbf{R}/\partial z)$ in β-CuZn ($\mathbf{u}$ is a unit vector). (a) $\mathbf{u}$ is parallel to b $=$ [111], thus $\mathbf{u}.(\partial\mathbf{R}/\partial z) = \partial\mathbf{R}_{//}/\partial z$.(*b*) $\mathbf{u} = [\bar{1}\bar{1}2]/\sqrt{6}$ is parallel to O*x*, whence $\mathbf{u}.(\partial\mathbf{R}/\partial z = \partial\mathbf{R}_{\perp}/\partial z)$. (*c*) u $=$ [001] and $\mathbf{u}.(\partial\mathbf{R}/\partial z) = (\partial\mathbf{R}_{//}/\partial z + (2/3)^{1/2}\partial\mathbf{R}_{\perp}/\partial z)$.

simulations. Saka [1] was the first to draw attention on the fact that, provided analyses be conducted under weak-beam conditions, the invisibility criterion can be safely applied, and that weak-beam images satisfactorily reflect the dislocation fine structure (we will see in Section 4.2 that anisotropy cannot be completely disregarded though).

Saka's conjecture has been investigated to some extent [25] in the case of β-CuZn which is cubic (bcc-based B2 structure) and whose anisotropy ratio, $A = 2c_{44}/(c_{11} - c_{12}) = 8$, is large. The issue regarding dislocation extinction under weak-beam conditions was examined by image simulation that confirmed the occurrence of extinction under $\mathbf{g}.\mathbf{b} = 0$. Conditions of image formation were then studied from maps of $(\partial\mathbf{g}.\mathbf{R}/\partial z)$ at constant $s_{\mathbf{g}}$. The former expression, which can be re-written as $\mathbf{g}.(\partial\mathbf{R}/\partial z)$, reflects the lattice distortion along the electron path projected along a direction selected from the diffraction pattern. A simplified way to account for anisotropic elasticity is to analyze the contribution of the displacement field normal to a screw dislocation, $\mathbf{R}_{\perp}\{\mathbf{R}_{y\perp}, \mathbf{R}_{z\perp}\}$, for this component vanishes in isotropic crystals (note that $\mathbf{g}.\mathbf{R}_{\perp}$ reduces to $\mathbf{g}.\mathbf{R}_{y\perp}$). Anisotropy effects are then manifested through the relative contributions of $\mathbf{g}.(\partial\mathbf{R}_{\perp}/\partial z)$ and $\mathbf{g}.(\partial\mathbf{R}_{//}/\partial z)$ to dislocation images.

The image of a dislocation comprises a dip and a tail component [11] which is why moderately anisotropic crystals imaged in bright- and dark-field near-Bragg conditions gives rise (i) to counterintuitive dislocation image symmetries and (ii) to a sometimes pronounced *residual* screw dislocation contrast under $\mathbf{g}.\mathbf{b} = 0$. As contrast arises from any crystal volume that is tilted off the Bragg condition, even of modest magnitude, the superimposition of a finite $\mathbf{R}_{\perp}$ may modify the tail component of the image of a dislocation considerably. What happens in weak-beam is that $\mathbf{R}_{\perp}$ being small, $\mathbf{g}.(\partial\mathbf{R}_{\perp}/\partial z)$ cannot be large enough to compensate for large lattice rotations and this eliminates the tail contribution. Furthermore, $\mathbf{g}.(\partial\mathbf{R}_{\perp}/\partial z)$ is quite smaller than $\mathbf{g}.(\partial\mathbf{R}_{//}/\partial z)$ so that it is essentially the latter quantity that determines image peak position.

The situation is a little more intricate for highly anisotropic crystals such as β-CuZn since the magnitudes of $\mathbf{g}.(\partial\mathbf{R}_{\perp}/\partial z)$ and $\mathbf{g}.(\partial\mathbf{R}_{//}/\partial z)$ are no longer significantly different [25]. This is illustrated by considering the three cases represented in Fig. 8 of the projection of $(\partial\mathbf{R}/\partial z)$ onto a selected unit vector, $\mathbf{u}$. Fig. 8a shows that the profile of $\partial R_{//}/\partial z$ ($\mathbf{u}_a = [111]/\sqrt{3}$) exhibits two vertical segments which by virtue of conditions (2) indicate some image reinforcement in this column. Fig. 8b ($\mathbf{u}_b = [\bar{1}\bar{1}2]/\sqrt{6}$) shows that in $\partial R_{\perp}/\partial z$, there are no such vertical regions and image intensity should be accordingly weak. It is noted that, given these unit vectors, $\partial R_{//}/\partial z$ is positive where $\partial R_{\perp}/\partial z$ is negative and vice versa. The unit vector $\mathbf{u}_c = [001]$ provides a combination of the two preceding fields, i.e. $\partial R_{[001]}/\partial z = \partial R_{//}/\partial z + (2/3)^{1/2}\,\partial R_{\perp}/\partial z$ (Fig. 8c). One can see that the horizontal lobe in Fig. 8a is largely cancelled out by $\partial R_{\perp}/\partial z$, leaving a V-shaped contour map that includes significantly elongated vertical segments. The images simulated for each case (where $\mathbf{g}$ now substitutes for $\mathbf{u}$) are fairly consistent, qualitatively, with the three profiles predicted from the CRW conditions (Section 3.1.1).

Finally, one may notice that regardless of crystal anisotropy and given $\mathbf{g}$, the contour maps remain self similar as $s_{\mathbf{g}}$ is varied. This property actually comes out analytically [25].

Although one cannot exclude though to encounter crystals where $\partial R_{\perp}/\partial z$ has more dramatic effects on weak-beam images of dislocations than what has been characterized for β-CuZn, it can be concluded that Saka's remark was largely founded.

4. Selected applications

4.1. Dipole heights

In cyclically deformed materials, the dislocation microstructure is remarkably self-organized. Copper single crystals deformed in single slip exhibit well-defined walls that contain a high density of dipolar configurations, essentially under the form of edge prismatic loops. A major issue in understanding and modelling fatigue properties in metals is that of loop formation. Elucidating the mechanisms thus involved necessitates a fair knowledge of loop distribution including height, length and loop type, that is, vacancy or interstitial. For small loop heights, the characterization must be conducted under weak-beam

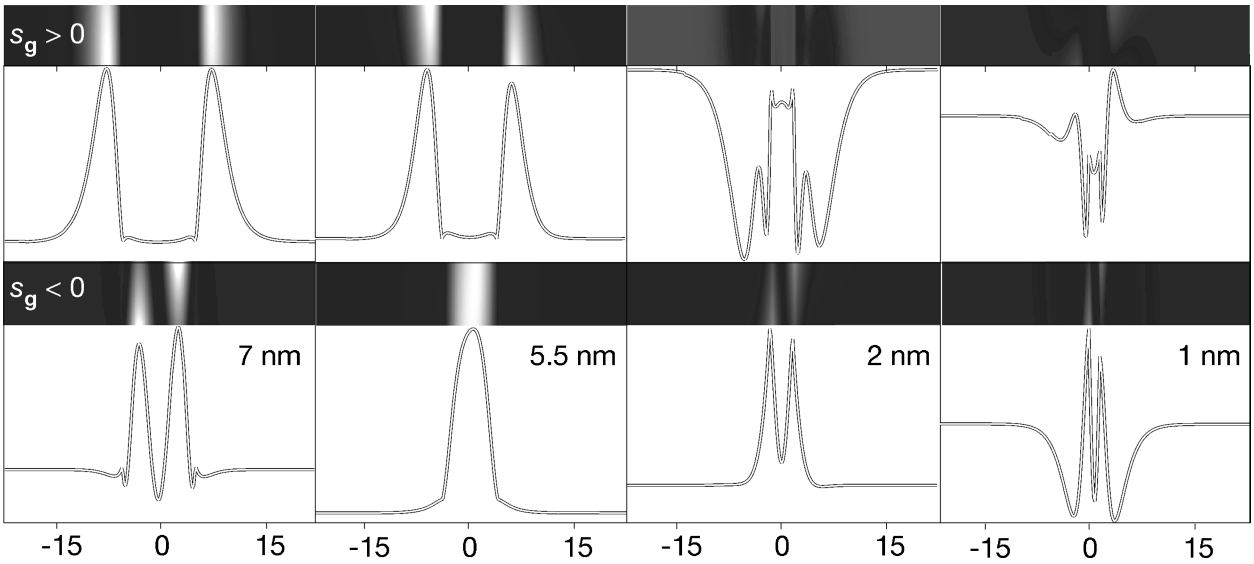

Figure 9 Dependence of the image width of an edge dipole in aluminium on the height of the dipole for **g** parallel to b for $s_{\mathbf{g}} = \pm 0.2\ \mathrm{nm}^{-1}$.

conditions. Loop length measurements cause no serious experimental problems whereas determining dipole nature is fairly complicated since this necessitates that the width variation of a given loop be checked in $\mathbf{g}/-\mathbf{g}$ experiments and monitored upon tilting [11]. It should be kept in mind that in fatigue walls, overlaps between images of neighbouring dipoles are, however, extremely frequent and subject to great variations upon tilting. Measuring dipole heights (i.e. distances between the slip planes of the two companion dislocations) is again a non trivial experiment. Since at equilibrium edge dipoles of undissociated dislocations are inclined 45° to the slip plane, the height of a dipole is equal to its width projected onto the slip plane. Antonopoulos *et al.* [30] have identified this width to the mean value of the broadened and narrowed images measured in a **g/-g** experiment, with **g** taken parallel to **b** and the slip plane parallel to the plane of observation. This method has been employed ever since. A lower limit for actual dipolar height y_{obs} of 3 nm has been reported in Cu [31], 2 nm in Ni [32], and down to 1 nm in AISI stainless steel [33] nearing the ultimate resolution in weak beam. This is what we discuss in the following.

We simulate dipole contrast under $s_{\mathbf{g}} = \pm 0.2\ \mathrm{nm}^{-1}$ for an accelerating voltage of 200 kV, as a function of dipole height, y_{true}, varied from 1 nm to about 7 nm (Fig. 9). For simplicity, we chose the case of aluminium where dislocation core spreading is at most 2–3 b [34]. For a 220 reflection in aluminium, the excursion from Bragg orientation corresponding to $s_{\mathbf{g}} = 0.2\ \mathrm{nm}^{-1}$ is achieved for the (**g**/4.25**g**) condition (Fig. 2). The image of an isolated dislocation ($\mathbf{b} = \pm\ 1/2[110]$) is shifted away from its geometrical projection by about 1.7 nm either way depending on the sign of the product $s_{\mathbf{g}}$ **g.b** (Fig. 3). Under the present choice for the sense of the line, the dipole image is the widest for $s_{\mathbf{g}} > 0$. The simulation indicates that the above averaging method works satisfactorily down to $y_{\mathrm{true}} \approx 6$ nm (e.g. one finds $y_{\mathrm{obs}} \approx 10.4$ nm and $\approx$ 7 nm for $y_{\mathrm{true}} = 10.6$ nm and $= 7.1$ nm, respectively). However, below a critical height y_c of 6 nm or so, averaging the pair of apparent dipole widths starts to be problematic because the images of the two dislocations simulated under $s_{\mathbf{g}} < 0$ show so much overlap that they cannot be resolved. There is therefore a range a dipole heights where the averaging method is inapplicable for image overlapping persists down to $y_{\mathrm{true}} \approx 2.1$ nm, below which the image again exhibits two separate peaks, while the wholesale signal has considerably weakened. It is worth pointing out that the peak corresponding to the right-hand side dislocation is now located on the left-hand part of the profile and vice versa. In this case, y_{obs}, taken as the average between the broad and narrow separations, is of course always overestimated (e.g. when $y_{\mathrm{true}} = 1.15$ nm then $y_{\mathrm{obs}} \approx (4.1 + 1.5)/2 = 2.3$ nm). Taking into account the image interchange yields $y_{\mathrm{obs}} \approx [4.1 + (-1.5)]/2 = 1.3$ nm, then consistent with y_{true} but the available signal is so much lessened that the measurement is not feasible in practice. As $s_{\mathbf{g}}$ is decreased, the critical dipole height y_c below which adverse overlapping effects take place is a function of $s_{\mathbf{g}}$. It increases as $s_{\mathbf{g}}$ decreases.

Further complications in determining dipole heights naturally arise in systems where dislocations are dissociated. This has been discussed very early by Carter and Holmes [35] in the case of faulted dipoles in Cu. Here a faulted dipole is a set of three adjacent fault strips exhibiting a Z-shaped cross-section and bordered outside by Shockley partial and stair-rods inside. Difficulties in interpreting weak-beam images of superimposed partials have been further emphasized in the case of Ni [36]. In the case of "perfect" dipoles, that is, dipoles comprised of a pair of dissociated dislocations, several causes of uncertainties may be encountered. Firstly, at equilibrium such dipoles should not assume the same 45° configuration as

for dipoles of perfect edge dislocations, this is especially true when the dipole height becomes of the order of or smaller than the separation between the companion partials. In Cu and Ni, the stacking fault width at equilibrium in the edge orientation amounts to 3.8 $\pm$ 6 nm [19] and 2.6 $\pm$ 0.8 nm [20], respectively, to be compared to the lowest dipole heights identified in these metals of 3 nm [16] and 2 nm [17], respectively. Second, for small dipole heights one may expect three possibilities for the coupling between the partials (leading/leading with the two trailing partials unpaired, or vice versa, or two pairs of leading/trailing partials). The real configuration may thus be significantly distinct from the assumption of a dipole of perfect dislocations that is usually made to estimate dipole heights.

To the author's knowledge, neither the limitations introduced by image overlaps in measuring small heights of dipoles of undissociated dislocations nor the issue related to the position of partial dislocations in the dissociated cases have been suitably discussed in the three materials where dipoles height measurements have been reported so far.

4.2. Dissociation distances

Measuring dissociation distances to derive the energy of some planar defect(s) requires certain precautions and corrections. As mentioned earlier, related issues had been thoroughly investigated for pairs of unlike partials when use of the weak-beam method was at its infancy. The case of two or more partials with identical Burgers vectors seems *a priori* less problematic for one would expect image shifts to be about the same for the partials. Based on the CRW criteria, a first attempt at elucidating this aspect has been made and analytical corrections derived by Doukhan in the case of spinel $MgAl_2O_4$ [37]. Later, observed separation distances have been somewhat carelessly made use of to determine surface defect energy, essentially APB energy, in intermetallics [38, 39]. The first serious analysis of the convoluted image of a pair of like partials is due to Baluc *et al*. [40, 41] who demonstrated the strong influence of elastic anisotropy and displacement field overlaps on the differences between observed and true dissociation distances in a Ni_3Al-based alloy. The correction was found as large as 10 and 30% for a dissociation on the $\{001\}$ and $\{111\}$ planes, respectively. These effects have been discussed at length for Ni_3Al-based alloy [12, 13, 42] where the ratio of APB energies on the $\{001\}$ and $\{111\}$ planes contributes to determine the conditions of dislocation locking which plays a pivotal role in the anomalous temperature dependence of the yield stress. It is noted that uncertainties on image shifts arising from the theoretical approximations involved in simulations have little influence, if any, for these uncertainties should contribute the same amount to both images.

A curious property may complicate APB energy determination [43]. It has been indeed observed that due to a large friction force exerted on partials on the cube plane, these cannot achieve full transition from the $\{111\}$ slip plane to the $\{001\}$ favourable cross-slip plane, in order to form the so-called Kear-Wilsdorf lock. What happens is that the configuration assumes a non-equilibrium configuration straddling the two planes. Since there is no need of a stair-rod like partials at the intersection between the two APB planes, the property can be detected only through tilting experiments. However, deriving an APB energy in this case is rather safe for every dislocation character but screw. In any orientation, lattice friction may make it difficult to ensure that this is an equilibrium configuration.

5. Physical properties of crystals exhibiting magnetic or atomic order

As exemplified in the above sections, the weak-beam method is essentially utilized to analyze and to resolve distortion fields in the vicinity of dislocations. Much less familiar is another application consisting in taking advantage of the contrast displayed by surface defects to measure physical properties such as the correlation length, ξ, in ordered alloys [21, 22] together with wall thickness in ferroelectric materials [23, 24]. In those cases, all what one considers are properties of the set of fringes observed under weak beam.

As to ferroelectric domain walls whose finite thickness is accounted for through a linear displacement field, thickness fringes are simulated by varying simultaneously the thicknesses of the sample, that of the domain wall, the deviation parameter $s_{\mathbf{g}}$ and absorption coefficients. Typically, a domain wall thickness of about 2.15 nm is derived by minimization of the mean square difference between simulated and experimental profiles.

In alloys undergoing a second-order phase transition, APB fringe contrast includes an attenuation function, itself dependent upon the correlation length. This enables the derivation of crystal parameters such as the correlation length, ξ, which itself scales with APB thickness, together with the temperature dependence of ξ below the critical transition temperature, T_c. What happens is that given $s_{\mathbf{g}}$ the fringe system fades out as ξ increases, and disappears at some specific value of ξ. Typically, disappearance occurs for a correlation length of 150 and 40 nm for ($\mathbf{g}$, $2\mathbf{g}$) and ($\mathbf{g}$, $5\mathbf{g}$), respectively. What makes the method quite convenient is that fringe contrast roughly which varies as $\exp[-2\pi^2 s_{\mathbf{g}}\xi]$, making the weak-beam images extremely sensitive to minute changes in $s_{\mathbf{g}}$ and/or ξ. Then *in situ* observations of APB fringes as a function of temperature for various ($\mathbf{g}$, $n\mathbf{g}$) conditions indicate that 20° below T_c, ξ is about 15 nm; it is 4 nm 35° below T_c [22]. In another experiment under fixed ($\mathbf{g}$, $4\mathbf{g}$) condition [21], a fit between experimental and simulated profiles was utilized to derive the correlation length dependence upon T_c

– T. The estimated values are similar to those found in [22], e.g. 5 nm for $T_c - T = 34$ K. The method is fully validated by the value of the critical exponent, ν in $\xi = [(T_c - T)/T]^{\nu}$, which amounts to 0.64 ± 0.1, very close indeed to its theoretical estimate of 0.63.

6. Concluding remarks

'Conditions' are not what guarantees good weak-beam pictures. Instead, it is highly recommended to favor a sound appreciation of the best experimental strategy that the features of interest may require. To improve image quality and defect visibility, safely conducted numerical image processing should not be dismissed. Admittedly, the quality of samples is of paramount importance and this requires outstanding skill and care during the preparation stage. Not the least requirement though for conducting defect analysis is imagination. In effect, the main difficulty in interpreting TEM images of *post mortem* deformed microstructures does not originate from contrast analysis but from the need to reconstruct the missing segment, that is, all that happened in the sample from the end of the thermomechanical treatment under investigation to the time the foil is ready for observation. That missing segment may have involved all sorts of artifacts. Similar issues are met during *in situ* experiments since then one has to wonder to what extent the proximity of free surfaces affects dislocation properties (such as cross-slip), hence to what extent *in situ* observations are representative of the mechanisms taking place in the bulk (see, however, [44]).

These are actually some of the factors that have made people prefer numerical experiments to TEM investigations. It is not so that simulations are artefact-free, but at variance from real crystals, numerical crystals accept simplifying assumptions which make it possible to study the implications of these assumptions one after the other. The potential of such a procedure is indeed quite fascinating, yet it has recently led to a new attitude where little is taken for certain if not observed in the computer. A numerical experiment is easily regarded as a solid proof. It is not infrequent though that the most spectacular simulations only reproduce mechanisms which, based on TEM observations and intuition, had been inferred two or three decades ago but forgotten since.

While multiscale computer simulations have flourished around the world in the last decade or so, expertise in experimental analysis of dislocations in real samples has gradually faded away. For reasons that are easy to figure out, the trend is irreversible.

Acknowledgments

The author is indebted to Drs Y.L. Chiu, D. Gratias and R. Schaüblin for invaluable discussions and advices at various levels of the writing of this paper.

References

1. H. SAKA, *Philosoph. Mag.* **49** (1984) 327.
2. C. J. HUMPHREYS and R. A. DRUMMOND, "The High Resolution Imaging of Defects, in *Electron Microscopy and Analysis*" (Institute of Physics, London, 1977) p. 241.
3. C. J. HUMPHREYS and R. A. DRUMMOND, "The Column Approximation and High Resolution Imaging of Defects, in Proceedings of the Sixth European Regional Conference on Electron Microscopy" (TAL International Publishing Company, Jerusalem, 1976) p. 142.
4. D. J. H. COCKAYNE, *Zeitschrift für Naturforschung a* **27A** (1972) 452.
5. D. B. WILLIAMS and C. B. CARTER, in Transmission Electron Microscopy (Plenum Press, New York and London, 1996).
6. P. VEYSSIÈRE and G. HUG, "The Use of Weak-Beam Dark-Field TEM in the Analysis of Defects in Intermetallics, in XIIth International Congress for Electron Microscopy", edited by E. Bailey (San Francisco Press: San Francisco, 1990) p. 450.
7. D. J. H. COCKAYNE, I. L. F. RAY and M. J. WHELAN, *Philosoph. Mag.* **20** (1969) 1265.
8. A. HOWIE, W. M. STOBBS and P. L. GAI, *Bulletin de la Société Française de Minéralogie et Cristallographie* **95** (1972) 690.
9. R. SANDSTRÖM, *Physica status Solidi (a)* **18** (1973) 639.
10. C. J. HUMPHREYS and R. A. DRUMMOND, in Proceedings of the Sixth European Regional Conference on Electron Microscopy (TAL International Publishing Company, Jerusalem, 1976) p. 142.
11. P. B. HIRSCH *et al*., "Electron Microscopy of Thin Crystals" (Butterworth, London, 1965).
12. K. J. HEMKER and M. J. MILLS, *Philosoph. Mag. A* **68**(2) (1993) 305.
13. K. J. HEMKER, *ibid.* **76**(1) (1997) 241.
14. C. J. HUMPHREYS *et al*., *ibid.* **35**(6) (1977) 1543.
15. Y. ISHIDA *et al*., *ibid.* **42** (1980) 453.
16. H. HEINRICH and G. KOSTROZ, *J. Micros.* **49**(1) (2000) 61.
17. J. M. WIEZOREK, A. R. PRESTON and C. J. HUMPHREYS, Column Approximation Effects on Partial Dislocation Weak Beam Images, in Institute of Physics Conference Series (IOP Publishing Ltd., 1995) p. 455.
18. P. VEYSSIÈRE and D. G. MORRIS, *Philosoph. Mag. Lett.* **66** (1992) 491.
19. F. GRÉGORI and P. VEYSSIÈRE, *Philosoph. Mag. A* **80**(12) (2000) 2913.
20. *idem*., *ibid.* **80**(12) (2000) 2933.
21. Y.-L. CHIU, *et al*., *Philosoph. Mag. Lett.* **83** (2003) 485.
22. B. VIGUIER and K. J. HEMKER, *Philosoph. Mag. A* **73**(3) (1996) 575.
23. W. J. TUNSTALL and P. J. GOODHEW, *Philosoph. Mag.* **13** (1966) 1259.
24. A. KORNER and H. P. KARNTHALER, *Philosoph. Mag. A* **44**(2) (1981) 275.
25. J. DOUIN, P. VEYSSIÈRE and G. SAADA, *ibid.* **77**(5) (1998) 1323.
26. R. SCHÄUBLIN and P. STADELMANN, *Mater. Sci. Engng.* **A 164** (199) 373.
27. C. BONTEMPS-NEVEU (University of Paris-Sud, 1991).
28. J. OLIVER (University of Paris-Sud., 1991).
29. P. VEYSSIÈRE and R. D. NOEBE, *Philosoph. Mag. A* **65** (1992) 1.
30. J. G. ANTONOPOULOS and A. T. WINTER, *Philosoph. Mag.* **33**(1) (1976) 87.
31. J. G. ANTONOPOULOS, L. M. BROWN and A. T. WINTER, *ibid.* **34**(4) (1976) 549.
32. B. TIPPELT, J. BRETSCHNEIDER and C. HOLSTE, *Physica Status Solidi (a)* **163** (1997) 11.
33. S. CATALAO *et al*., *Mater. Sci. Engng.* **A400–401** (2005) 349.
34. M. J. MILLS and P. STADELMANN, *Philos. Mag. A* **60** (1989) 355.

35. C. B. CARTER and S. M. HOLMES, *Philosoph. Mag.* **32** (1975) 599.
36. *idem*, *ibid.* **35**(5) (1977) 1161.
37. N. DOUKHAN, R. DUCLOS and B. ESCAIG, *Journal de Physique* **40** (1979) 381.
38. P. VEYSSIÈRE, J. DOUIN and P. BEAUCHAMP, *Philosoph. Mag. A* **51** (1985) 469.
39. P. VEYSSIÈRE, *ibid.* **50** (1984) 189.
40. N. BALUC, H. P. KARNTHALER and M. J. MILLS, *Philosoph. Mag. A* **64**(1) (1991) 137.
41. N. BALUC, R. SCHAÜBLIN and K. J. HEMKER, *Philosoph. Mag. Lett.* **64**(5) (1991) 327.
42. N. BALUC and R. SCHÄUBLIN, *Philosoph. Mag. A* **74**(1) (1996) 113.
43. C. BONTEMPS and P. VEYSSIÈRE, *Philosoph. Mag. Lett.* **61** (1990) 259.
44. A. COURET, J. CRESTOU, S. FARENC, G. MOLENAT, N. CLEMENT, A. COUJOU and D. CAILLARD, *Microsc. Microanal. Microstr.* **4** (1993) 153.